Provided for non-commercial research and education use.
Not for reproduction, distribution or commercial use.

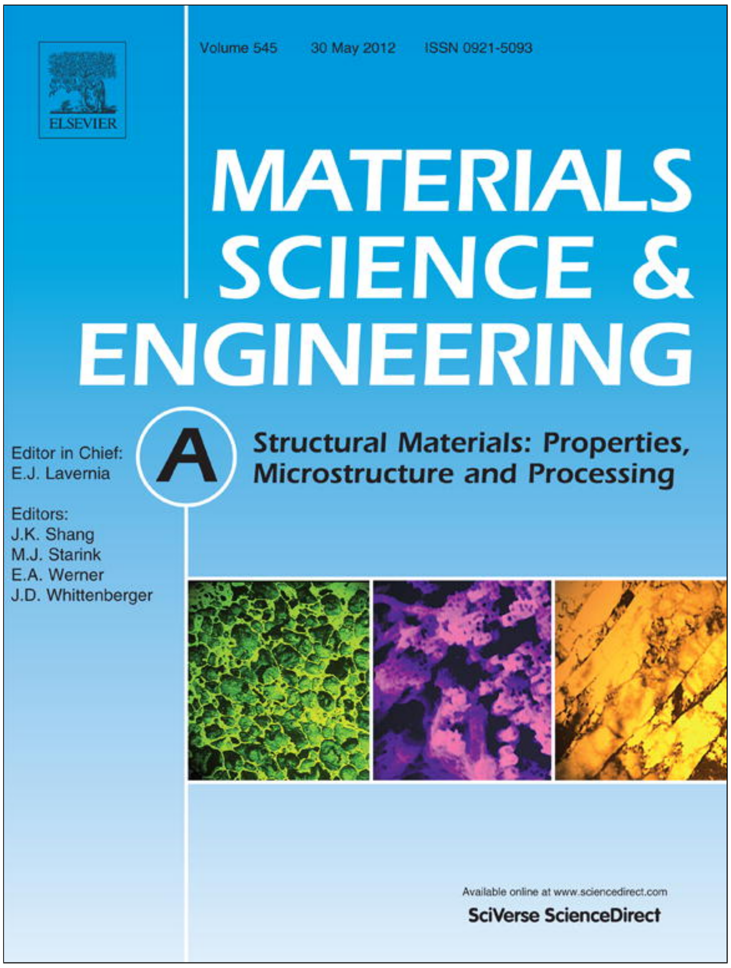

Volume 545 30 May 2012 ISSN 0921-5093

ELSEVIER

MATERIALS SCIENCE & ENGINEERING

A

Structural Materials: Properties, Microstructure and Processing

Editor in Chief:
E.J. Lavernia

Editors:
J.K. Shang
M.J. Starink
E.A. Werner
J.D. Whittenberger

Available online at www.sciencedirect.com
SciVerse ScienceDirect

This article appeared in a journal published by Elsevier. The attached copy is furnished to the author for internal non-commercial research and education use, including for instruction at the authors institution and sharing with colleagues.

Other uses, including reproduction and distribution, or selling or licensing copies, or posting to personal, institutional or third party websites are prohibited.

In most cases authors are permitted to post their version of the article (e.g. in Word or Tex form) to their personal website or institutional repository. Authors requiring further information regarding Elsevier's archiving and manuscript policies are encouraged to visit:

http://www.elsevier.com/copyright

Author's personal copy

Materials Science and Engineering A 545 (2012) 168–175

Contents lists available at SciVerse ScienceDirect

Materials Science and Engineering A

journal homepage: www.elsevier.com/locate/msea

Effective X-ray elastic constant measurement for in situ stress measurement of biaxially strained AA5754-O

Mark A. Iadicola [a,*], Thomas H. Gnäupel-Herold [b]

[a] Metallurgy Division, 100 Bureau Drive, STOP 8553, National Institute of Standards and Technology, Gaithersburg, MD 20899, USA
[b] NIST Center for Neutron Research, 100 Bureau Drive, STOP 6102, National Institute of Standards and Technology, Gaithersburg, MD 20899, USA

ARTICLE INFO

Article history:
Received 21 September 2011
Received in revised form 27 February 2012
Accepted 29 February 2012
Available online 14 March 2012

Keywords:
X-ray diffraction
Aluminum alloys
Sheet forming
Plasticity
Residual stresses
Neutron diffraction
Intergranular strain

ABSTRACT

Accurate measurement of stresses by X-ray diffraction requires accurate X-ray elastic constants. Calibration experiments are one method to determine these for a specific material in a specific condition. In this paper, uniaxial tension experiments are used to investigate the variation of these constants after uniaxial and equal-biaxial plastic deformation for an aluminum alloy (AA5754-O) of interest to the automotive industry. These data are critical for accurate measurement of the biaxial mechanical properties of the material using a recent experimental method combining specialized sheet metal forming equipment with portable X-ray diffraction equipment. The measured effective X-ray elastic constants show some minor variation with increased plastic deformation, and this behavior was found to be consistent for both uniaxially and equal-biaxially strained samples. The use of two average values for effective X-ray elastic constants, one in the rolling direction and one transverse to the rolling direction of the sheet material, is shown to be of sufficient accuracy for the combined tests of interest. Comparison of uniaxial data measured using X-ray diffraction and standard methods show good agreement, and biaxial stress–strain results show good repeatability. Additionally, the calibration data show some non-linear behavior, which is analyzed in regards to crystallographic texture and intergranular stress effects. The non-linear behavior is found to be the result of intergranular stresses based on comparison with additional measurements using other X-ray diffraction equipment and neutron diffraction.

Published by Elsevier B.V.

1. Introduction

The mechanical response of sheet metals to large strains in biaxial tension (e.g., uniaxial, plane strain, and equal-biaxial strains) is of interest to the metal forming community. Many testing configurations exist to achieve some or all of the tensile strain states of interest including cylindrical tension-torsion-inflation, inflation bulge, hemispherical or flat ram, and cruciform testing, but all have inadequacies resulting from out of plane bending, application of non-uniform deformation, limited strain range, or the need for assumed constitutive laws to determine the stress in the sample. Iadicola et al. [1] used a combination of biaxial mechanical testing and X-ray diffraction (XRD) techniques to produce less ambiguous stress–strain measurements up to large plastic (strains > 15%) in-plane (biaxial) stretching of an as-received sheet metal sample. In this method of testing, XRD is used to measure the in situ inter-atomic lattice spacing in the sheet which is proportional to the stress through effective X-ray elastic constants (XECs). This method requires careful calibration, but removes the need for numerical modeling with an assumed constitutive law to determine the stress–strain behavior. In this paper, the calibration measurements of effective XECs for the biaxial experiments in Iadicola et al. [1] are described, with special attention to the possibility of effective XEC variation due to the macroscopic plastic strain history. Preliminary work on these measurements was presented briefly in Iadicola and Gnaeupel-Herold [2], but has been substantially extended here.

In this work, elastic uniaxial loading is used in conjunction with established XRD techniques to determine effective XECs for one material of interest. These experiments are performed on as-received material and material deformed equal-biaxially to various strain levels in a manner similar to Iadicola et al. [1]. Due to the orthotropic nature of the rolled sheet metal, the experiments are performed for samples in both the rolling direction (RD) and transverse to the rolling direction (TD).

2. Material & mechanical testing procedure

The material used in this investigation is commercially available 1 mm thick AA5754-O (which is of interest to the automotive industry). The microstructure of the as-received sheet shows recrystallized grains, which are relatively equiaxed in the rolling

---

* Corresponding author. Tel.: +1 301 975 5703; fax: +1 301 975 4553.
E-mail addresses: mark.iadicola@nist.gov (M.A. Iadicola), gnaeupel@nist.gov (T.H. Gnäupel-Herold).

0921-5093/$ – see front matter. Published by Elsevier B.V.
doi:10.1016/j.msea.2012.02.100

Author's personal copy

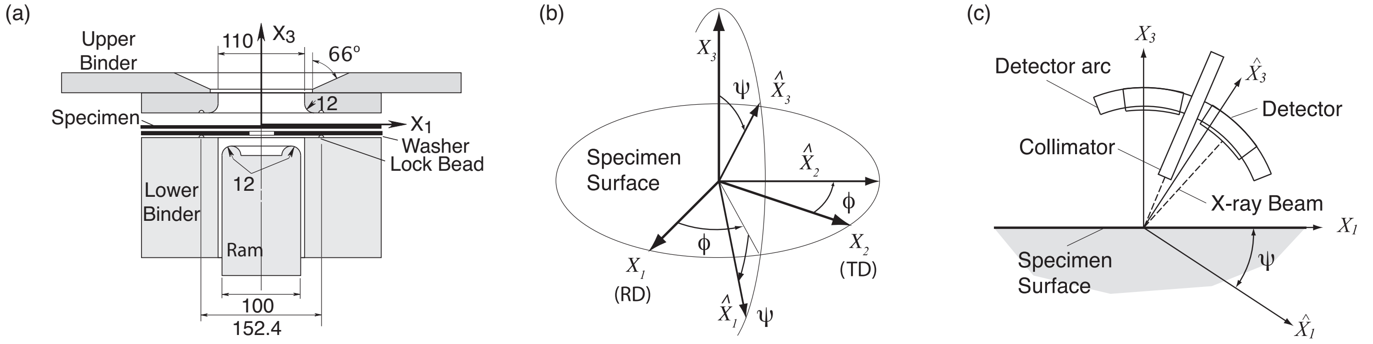

Fig. 1. Specimen and XRD axes defined by (a) through section of axisymmetric Marciniak tooling (dimensions in mm), (b) standard XRD angles, and (c) sketch of the XRD head.

plane, but slightly elongated when viewed in the transverse plane. The size of the grains is relatively uniform in each direction, with an average diameter of 40 μm in the normal plane.

The effective XEC calibration experiments presented here use uniaxial tensile tests, of both as-received and equal-biaxially strained samples, in conjunction with XRD measurements to calibrate the effective XEC. A portable uniaxial testing frame is used to test ASTM-E8 sub-sized sheet metal specimen shape samples with a reduced tab length. During deformation, load (from a calibrated load cell) and strain (from a calibrated axial extensometer) are measured to determine the true stress in the gage section. At selected strain levels the specimen is unloaded (to a stress never less than 80% of the as-received initial uniaxial yield stress, approximately 94 MPa for the RD) and reloaded elastically. During these elastic unload/reload times, the uniaxial loading is paused at multiple points and XRD is used to measure the current interatomic lattice spacing. These experiments are performed on as-received samples and equal-biaxially strained samples (as in Iadicola et al. [1]) with approximately 5%, 10%, 15%, and 20% equal-biaxial true-strain, in both RD and TD.

The method of specimen deformation used here to perform the equal-biaxial straining is a variation [3] of the Marciniak flat bottom ram test [4] (Fig. 1a is a through section drawing of the axisymmetric tooling), which imposed near-linear strain paths in a range of strain states from uniaxial to equal-biaxial tension (under plane stress conditions on as-received sheets, stretching the sheet like a drum head). The upper surface of the specimen is exposed for metrology. In Iadicola et al. [1], biaxial stress–strain behavior was measured using a combination of this mechanical deformation and XRD to determine stress. A washer of mild steel is used to reinforce the specimen where it will bend around the ram radius, thus concentrating the deformation in the center of the specimen directly above the centerline of the ram. The upper and lower surfaces at this center section are traction free. The ram force cannot be simply related to the resulting in-plane stresses in this center section of the sheet, therefore XRD is used to measure the in situ interatomic lattice spacing, which is proportional to the in situ stresses in the sheet through an effective XEC.

The procedure used in Iadicola et al. [1] is similar to that used to calibrate the effective XEC. We briefly review the procedure here. In Iadicola et al. [1], after as-received sheet and reinforcing washer are initially clamped in the forming machine binder (or locked in the grips for the uniaxial experiments), the general procedure includes three steps: (1) the material is loaded by imposing tensile strains (by an increase in ram height for biaxial loading or by a crosshead displacement for uniaxial loading) at a quasi-static rate, (2) the displacement is held fixed and the XRD system is focused on the surface of the sheet, and (3) an XRD scan (described below) is performed. This procedure is then repeated for the next data point. For both the experiments in Iadicola et al. [1] and in this work, the entire procedure (1 through 3) takes approximately 8 min (due in large part to the low power of the XRD system and X-ray absorption by the sample). The macroscopic strain during this hold time is calculated by averaging the output of an extensometer for the entire scan time (standard deviations in these data were typically <0.005% strain). The biaxial experiments use a biaxial extensometer with similar performance to the axial extensometer used in the uniaxial experiments.

3. XRD procedure

A portable low-power (60 W) XRD system is mounted to the back of the biaxial sheet metal forming machine, and is used to measure the interatomic lattice spacing in the exposed top surface of the specimen as described in [5]. The system uses the $\sin^2\psi$-method [[6], pp. 122 ff.] in the ψ-geometry (Fig. 1b and c), with interchangeable single source X-ray tubes. The two coordinate systems in Fig. 1b are the material system and the XRD-head system. The material system is oriented with the X_1 axis in the RD, X_2 in the TD, and X_3 vertical to the sheet. The XRD system ($\hat{X}$) is offset to the material system first by a rotation (ϕ) about the sheet normal and then by a rotation (ψ) about the $\hat{X}_2$ axis, where the $\hat{X}_3$ axis is the bisector of the X-ray source and reflected beams. Fig. 1c is a sketch XRD-head (X-ray source beam with left and right detectors shown) and the axes for one ψ-angle at $\phi = 0$. In this figure, the $\hat{X}_3$ axis is oriented in the direction associated with the measurements using the right detector. Due to the space constraints, this system only permits tilting in one direction with respect to the specimen (ϕ = constant) over a limited angle range ($\psi = \pm 35^\circ$).

In this work, as well as in Iadicola et al. [1], Co Kα radiation is used. The beam is collimated and passed through a 5 mm long and 1.5 mm wide (in the ψ-tilt direction) aperture. The diffracted/reflected X-rays from the specimen are acquired by two 256 channel 10° linear position sensitive scintillation detectors (one placed symmetrically on each side of the source beam). Note that Fig. 1c shows both detectors, but the axes as shown are for the source beam and right detector only. The system is configured to acquire a single reflection peak profile in each detector at one time, and here the $\{420\}$ family of planes (Bragg angle $\theta = 81.25^\circ$ for the Co X-ray source) is used exclusively. The profiles are fit using a two peak (Kα_1 and Kα_2) Pearson's VII function (with an exponent of 1.77) to the upper 85% of the total peak after background subtraction. Lattice spacing ($d_{\phi\psi}$) is computed from the peak position through Bragg's Law. The stress free lattice spacing (d_o) is not measured directly for the material, since the $\sin^2\psi$-method is not very sensitive to error in this value, and a system default value for aluminum is assumed. To verify this, an XRD measurement of a stress free powder is made, and the assumed d_o is considered acceptable if the measured lattice strains are less than

Author's personal copy

the systematic uncertainty ($\pm 9\times 10^{-5}$ strain). For all of the XRD measurements reported here, 26 ψ-angles (13 for each detector) are used for each XRD scan. To reduce the effect of random noise and improve the quality of the peak profile in light of grain size and crystallographic texture, each peak profile is scanned for about 15 s during which a small ($\pm 3^\circ$) ψ-angle oscillation is performed. The approximate penetration depth is 40 µm, resulting in about 4500 grains diffracting at any given time, but only a few of these will be properly oriented for the {4 2 0} reflection at any given tilt.

The standard governing equation [[6], p. 118 Eq. (5.4)] relating the lattice strain (based on the reference and measured lattice spacing) to the surface strains (ε_{ij}) rotated to the specimen surface system (Fig. 1b) is

$$\frac{d_{\phi\psi}-d_o}{d_o}=\varepsilon_{11}\ \cos^2\phi\sin^2\psi+\varepsilon_{12}\sin 2\phi\sin^2\psi+\varepsilon_{22}\sin^2\phi\sin^2\psi+\varepsilon_{33}\cos^2\psi+\varepsilon_{13}\cos\phi\sin 2\psi+\varepsilon_{23}\sin\phi\sin 2\psi. \qquad (1)$$

An isotropic constitutive law is assumed as is typical for the $\sin^2\psi$-method. Additionally, the top and bottom surfaces of the specimen are stress free in the center section (this is true for the uniaxial case and for the biaxial case above the center of the ram, i.e., the washer hole), therefore we neglect the through thickness stress ($\sigma_{33}=0$). When considering the above assumptions and tilting in the rolling direction ($\phi=0$) Eq. (1) becomes,

$$\frac{d_\psi-d_0}{d_0}=\frac{1}{2}S_2\sigma_{11}\ \sin^2\psi+S_1(\sigma_{11}+\sigma_{22})+\frac{1}{2}S_2\sigma_{13}\ \sin 2\psi \qquad (2)$$

where σ_{ij} are the components of stress in the surface system, and S_1 and $(1/2)S_2$ are the effective XECs. If tilting in the transverse direction ($\phi=90^\circ$), the σ indices 1 and 2 in Eq. (2) are exchanged. Ideally $S_1=-\nu/E$ and $(1/2)S_2=(1+\nu)E$, but the effective constants actually vary with the chosen family of planes and the specific material. For example, reported values of $(1/2)S_2$ [[6], Appendix F] for pure aluminum and AA5083-H23 for the {4 2 0} family of planes using Co Kα radiation differ by 11%. Additionally, it seems reasonable to assume the effective XECs may differ for RD and TD, due to the orthotropic nature of rolled sheet metal; therefore we will investigate calibration of the effective XECs in both of these directions. Only the first term on the right hand side of Eq. (2) is used here to determine σ_{11}. The first term captures this value as proportional to the slope of the $\sin^2\psi$ behavior. Additionally, the XRD system combines the data from the two detectors by resetting the intercept of the linear lattice strain versus $\sin^2\psi$ to zero for both detectors, which prevents accurate calculation of the second term on the right hand side of Eq. (2). In both this work and Iadicola et al. [1], the stress in the ψ-tilt direction (σ_{11} in Eq. (2)) is of primary interest, so only the $(1/2)S_2$ effective XEC is needed. The third term ('splitting' term) is expected to be zero, since the top and bottom surfaces are stress free in the normal direction and the measurements are made after initial plastic yield throughout the thickness. Potential causes of divergence from linear behavior, due to texture or intergranular stresses, will be discussed in the next section.

The calibration experiments permit measurement of the true-stress in the axial direction at any given extension hold, while all other macroscopic stresses are zero. Combining these data with the XRD data at these extension holds, Eq. (2) can be solved for $(1/2)S_2$ (the effective XEC of interest). These data are developed for as-received and equal-biaxial strained samples in both the RD and TD for a range of macroscopic strain levels to verify orientation and deformation induced effective XEC variation.

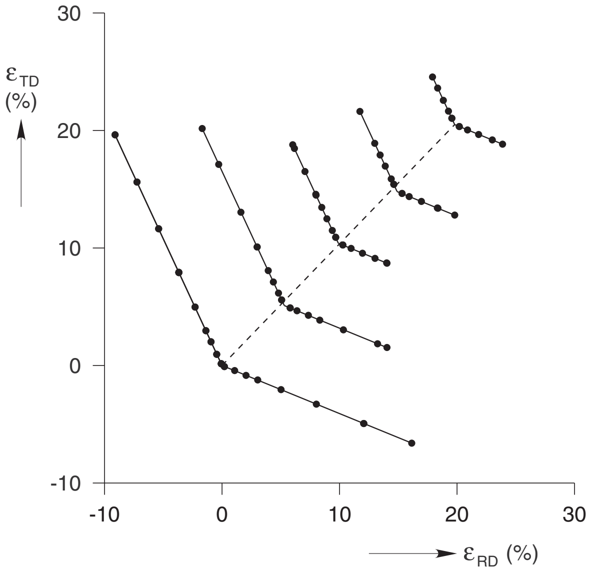

Fig. 2. Matrix of effective XEC uniaxial calibration unload/reload cycles (points) plotted on true-strain axes. Dashed line shows the equal-biaxial strain path from as-received condition to start of uniaxial tests.

4. Results and analysis

4.1. Effective XEC results

For each of the five equal-biaxial strain levels (including as-received) and in each direction (RD and TD) a uniaxial effective XEC experiment is performed with 5 to 9 elastic unload/reload series at various strain levels resulting in almost 70 independent measurements of effective XEC. Fig. 2 plots the matrix of experiments where each data point represents one unload/reload calibration measurement set at a given true-strain in RD and TD. The uncertainty of these strain values is much smaller than the data symbols shown. The dashed line in the figure represents the equal-biaxial strain path. Fig. 3a plots the lattice strain versus $\sin^2\psi$ behavior for one series, and the linear fits to these data. The slopes of these fits are plotted in Fig. 3b versus the measured true-stresses, and this is also fit with a line where the slope is the effective XEC $(1/2)S_2$ for this elastic unload/reload. The uncertainty for each $(1/2)S_2$ value is calculated from the propagation of the lattice strain uncertainty, that is approximately $\pm 9\times 10^{-5}$ strain based on the system uncertainty. Fig. 4a and b plots the calculated $(1/2)S_2$ values (with uncertainties shown as error bars) versus the hardening stress and plastic strain, respectively, for the as-received sample (with RD in red filled circles and TD in blue open squares). Large variations in effective XEC are seen for hardening stress and plastic strain near the yield offset stress of 94 MPa and the initial 0.2% yield offset. At these low stresses and strains, the calculated uncertainties (from the propagated uncertainties) are quite large, and exceed the variation seen in effective XEC. This is partially due to the small range of stress over which the linear fit is being calculated. In the figures, calculated $(1/2)S_2$ values for the uniaxial calibration experiments of previously equal-biaxially strained samples are also shown. Differences between RD and TD values (solid and open symbols, respectively) are even less distinct, but the trend for all the points seems to show a slight trend between effective XEC and hardening stress or plastic strain during plastic deformation, irrespective of the method of plastic deformation (uniaxial or equal-biaxial), although the higher stress and plastic strain levels are only achievable with biaxial deformation. A few outlier points exist, but these are associated with elastic unload/reload cycles near or just after necking where the uniaxial stress-state assumption breaks down. The overall

Author's personal copy

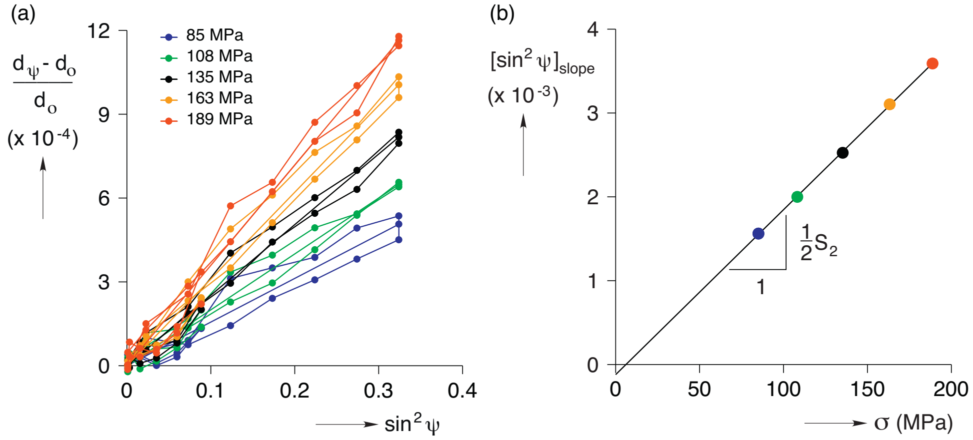

Fig. 3. Calibration experiment results for as-received TD (a) sin^2 ψ behavior and (b) the associated effective XEC determination from the slope of linear fits in (a).

average $(1/2)S_2$ values for RD and TD are 19.3 TPa^{-1} and 19.7 TPa^{-1}, respectively. Apparently the orthotropic nature of the rolled sheet does not result in a very substantial difference in the XECs in the RD and TD.

In Fig. 3a, there is some variation from the linear sin^2 ψ behavior, which in part is due to random errors within the systematic uncertainty. These are present even when measuring the stress free powder samples, which may be used to bound these errors to $\pm 9 \times 10^{-5}$ lattice strain. Some samples in this study, particularly after equal-biaxial straining, have lattice strain variations that deviate from linearity by values slightly greater then these bounds, and in some cases seem to follow a pattern (similar to a wave form). This could be a result of other issues, such as texture or intergranular stresses so these are now discussed.

4.2. Non-linear sin^2 ψ behavior

Although crystallographic texture has been shown to be an important factor in non-linear sin^2 ψ behavior in some materials (e.g., iron and steels), the non-linear sin^2 ψ behavior seen here cannot be explained by the effects of preferred orientation. The full extent of the texture effect on the X-ray elastic constants in aluminum was investigated using the inverse Kröner model [7] together with the crystal orientation distribution function (ODF). Details of the calculation of X-ray elastic constants using the ODF can be found in [7]. The ODF was determined from measured X-ray pole figures ((2 0 0), (2 2 0), (1 1 1) reflections) using the program popLA [8]. Fig. 5 plots the calculated lattice strains for an applied uniaxial stress of 100 MPa for a uniform crystallographic texture distribution (with $(1/2)S_2 = 19.3$ TPa^{-1}), for the measured as-received ODF, for the ODF measured after 5% equal-biaxial straining, and for the ODF measured after 20% equal-biaxial straining. Also plotted in the figure are the measured lattice strain data for a uniaxial calibration sample in the TD after 5% equal-biaxial strain at a true-stress of 100 MPa. Recall that the systematic uncertainty is estimated at $\pm 9 \times 10^{-5}$ lattice strain. The results in Fig. 5 demonstrate the effect of the texture induced non-linear behavior of the XEC is very small even for the sample with the highest strain (20% equal-biaxial strain). The calculated non-linear behavior is much less than the non-linear behavior seen in the data and does not follow the same trends.

The other source of variations from linearity considered here is intergranular stress, which is difficult to measure. Initial assessment of intergranular stresses was performed using the calibration data developed here. The results led to further study using another XRD system as well as measurement through neutron diffraction. We will discuss each method in turn, and compare the results.

First the calibration data was analyzed. If we assume intergranular stresses add an offset strain (ε_{int}) to the average lattice strain ($\bar{\varepsilon}$) during a single XRD scan then the measured lattice strain is $\varepsilon = \bar{\varepsilon} + \varepsilon_{int}$ [9], where $\bar{\varepsilon}$ equals the right hand side of Eq. (2). This formulation assumes the ε_{int} values are not stress level dependent, but are added to the average lattice strain (which is dependent on the average stress). The ε_{int} values are dependent on the particular

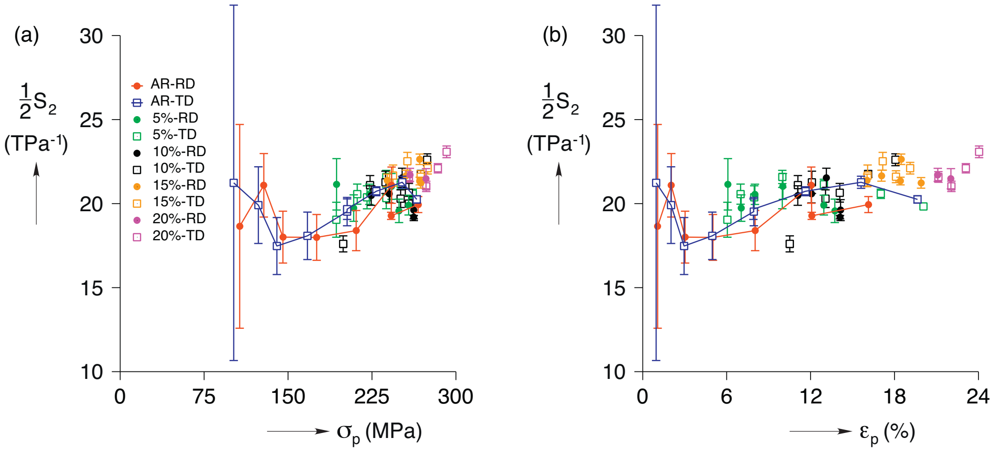

Fig. 4. Variation of effective XEC $(1/2)S_2$ with plastic deformation, shown versus (a) hardening stress and (b) plastic strain.

Author's personal copy

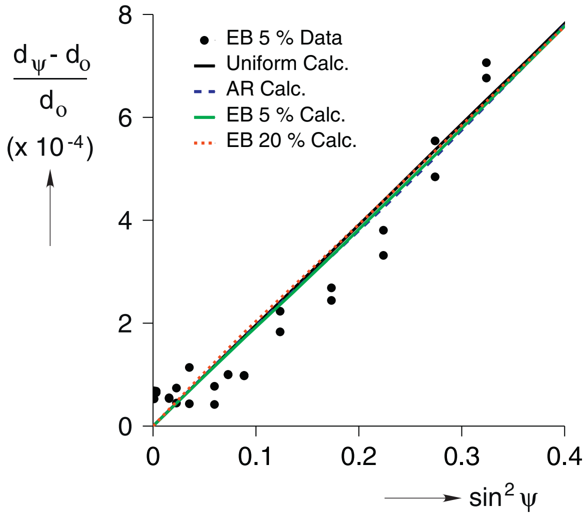

Fig. 5. Inter-atomic lattice strain data (circles) versus $\sin^2\psi$ for uniaxial sample in TD after 5% equal-biaxial straining at applied true-stress of 100 MPa. Calculated lattice strains (lines) versus $\sin^2\psi$ at 100 MPa for uniaxial TD sample with uniform crystallographic texture distribution, as-received (AR) texture, texture after 5% equal-biaxial (EB 5%) and 20% equal-biaxial (EB 20%) straining.

crystallites (and the difference in the yield stress between adjacent grains) diffracting at the current tilt and rotation angles, therefore ε_{int} would be a function of ψ-angle and ϕ-angle. In this work we are also admitting the possibility of variation with plastic strain (ε_p) as well, thus Eq. (2) becomes,

$$\frac{d_\psi - d_0}{d_0} = \frac{1}{2}S_2\sigma_{11}\sin^2\psi + S_1(\sigma_{11}+\sigma_{22}) + \frac{1}{2}S_2\sigma_{13}\ \sin 2\psi + \varepsilon_{\text{int}}(\psi, \phi = 0, \varepsilon_p). \qquad (3)$$

Recall that at each $\sin^2\psi$ scan, the intercept of the linear fit was set to zero, this effectively assumes that there is a constant d_o that exists for all the ψ-angles (and allows for combination of the data from the two detectors). In the absence of intergranular strains, the variation of measured strain with applied stress should intercept at zero. This does not occur exactly, due to random and systematic errors (as seen when measuring a stress-free powder sample). For a uniaxial stress state with intergranular stresses Eq. (3) simplifies to,

$$\frac{d_\psi - d_0}{d_0} = \left(\frac{1}{2}S_2\sin^2\psi + S_1\right)\sigma_{11} + \varepsilon_{\text{int}}(\psi, \phi = 0, \varepsilon_p). \qquad (4)$$

This suggests that the strain associated with intergranular stress may be determined from the intercept of a linear fit of the lattice strains to the applied uniaxial stress for a fixed combination of ϕ and ψ for one elastic unload/reload cycle (ε_p is constant). Fig. 6 shows the results and analysis for one uniaxial effective XEC experiment in the TD on a 5% equal-biaxial strained sample. Fig. 6a plots the mechanical response (black line) with circle symbols at the time in the load history that each XRD scan is performed. Fig. 6b shows the determination of the intergranular strains as a perspective plot where the black dashed lines are described by Eq. (4) for two ψ-angles and the intercepts with the $\sigma_{11} = 0$ plane are the ε_{int} values for the given TD ($\phi = 90°$) and the ψ-angles. The data in Fig. 6b are color coded to the points in Fig. 6a (above the 94 MPa threshold) during the first loading after the equal-biaxial straining. Fig. 7a shows lattice strain versus stress for $\psi = -34.7°$ (in the TD for the 5% equal-biaxial strained sample). The non-zero intercept of the linear fit is partially due to intergranular stresses. Fig. 7b is the distribution of these values with ψ-angle for the same sample (error-bars are the propagated uncertainty). There are points with slightly (but distinctly) larger amplitude than the powder sample level ($\pm 9 \times 10^{-5}$), suggesting this behavior is more than random or systematic error. Analyzing the data from the entire matrix of calibration experiments, similar behavior is seen for the initial loading

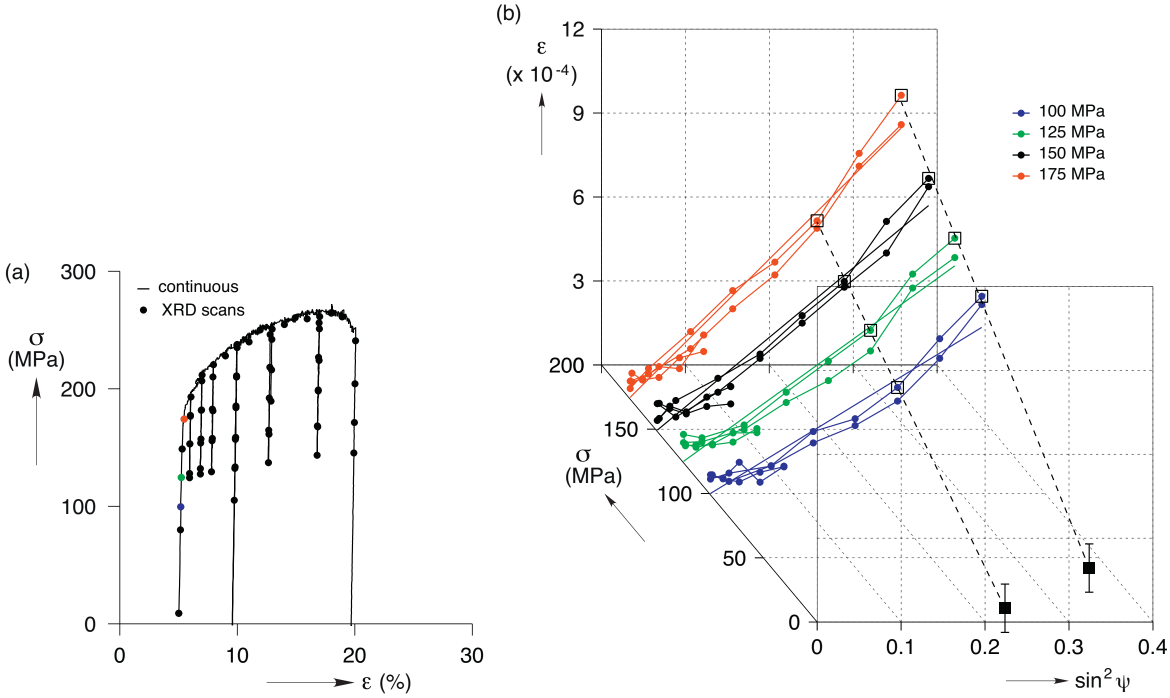

Fig. 6. (a) Uniaxial true-stress versus true-strain curve in TD after 5% equal-biaxial straining. Data from load cell and extensometer shown as a solid line with circles at the times of the XRD scans. (b) Inter-atomic lattice strain versus $\sin^2\psi$ at various elastic stress levels in (a) plotted along the applied true-stress. Black squares are calculated ε_{int} and dashed lines are fits to Eq. (4) at $\psi = -34.7°$ and $-28.23°$.

Author's personal copy

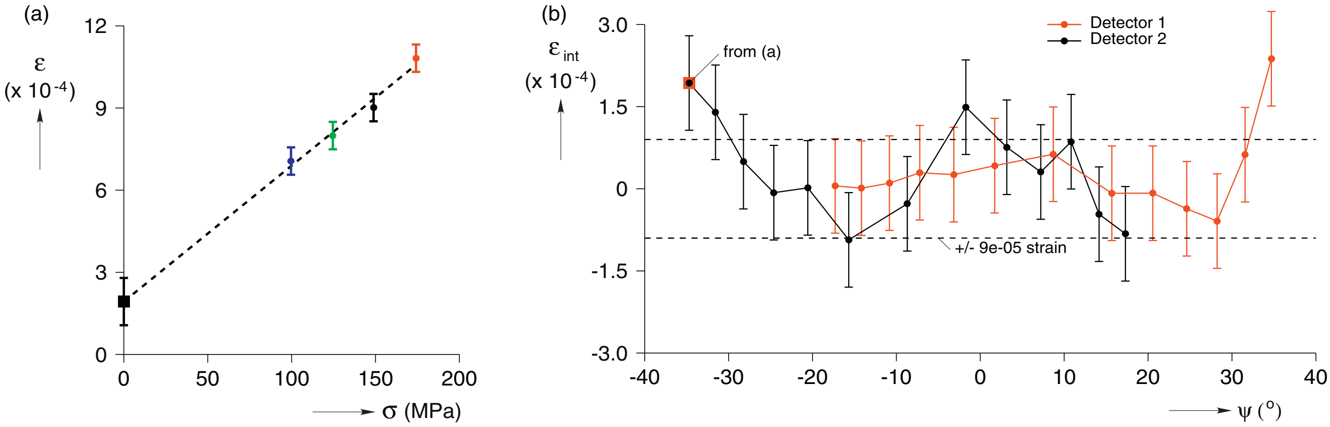

Fig. 7. Example of intergranular strain data analysis: (a) lattice strains versus stress at $\psi = -34.7°$ with linear intercept at the calculated intergranular strain value (from Fig. 6b) and (b) intergranular strain variation with ψ-angle for TD sample after 5% equal-biaxial straining.

of the equal-biaxially strained samples and not for the as-received samples. After initial uniaxial plastic deformation, the intergranular strains seem to reduce to below the $\pm 9 \times 10^{-5}$ bounds for almost all samples, but some distinctly negative strains seem to develop near $\psi = \pm 15°$ in multiple cases. Recalculation of the $(1/2)S_2$ values after subtraction of the calculated intergranular strains results in values similar (less than 0.5% difference) to those shown in Fig. 4.

The sudden increase in lattice strains at the edge of the tilt range in Fig. 7b suggested that a review of the intergranular strains over a larger ψ range was needed to verify the behavior. Therefore measurements of an unloaded sample equal-biaxial strained to approximately 25% strain were taken using a XRD system with Euler goniometer that can measure tilts to almost $\psi = \pm 70°$, well beyond the limited range of the XRD system

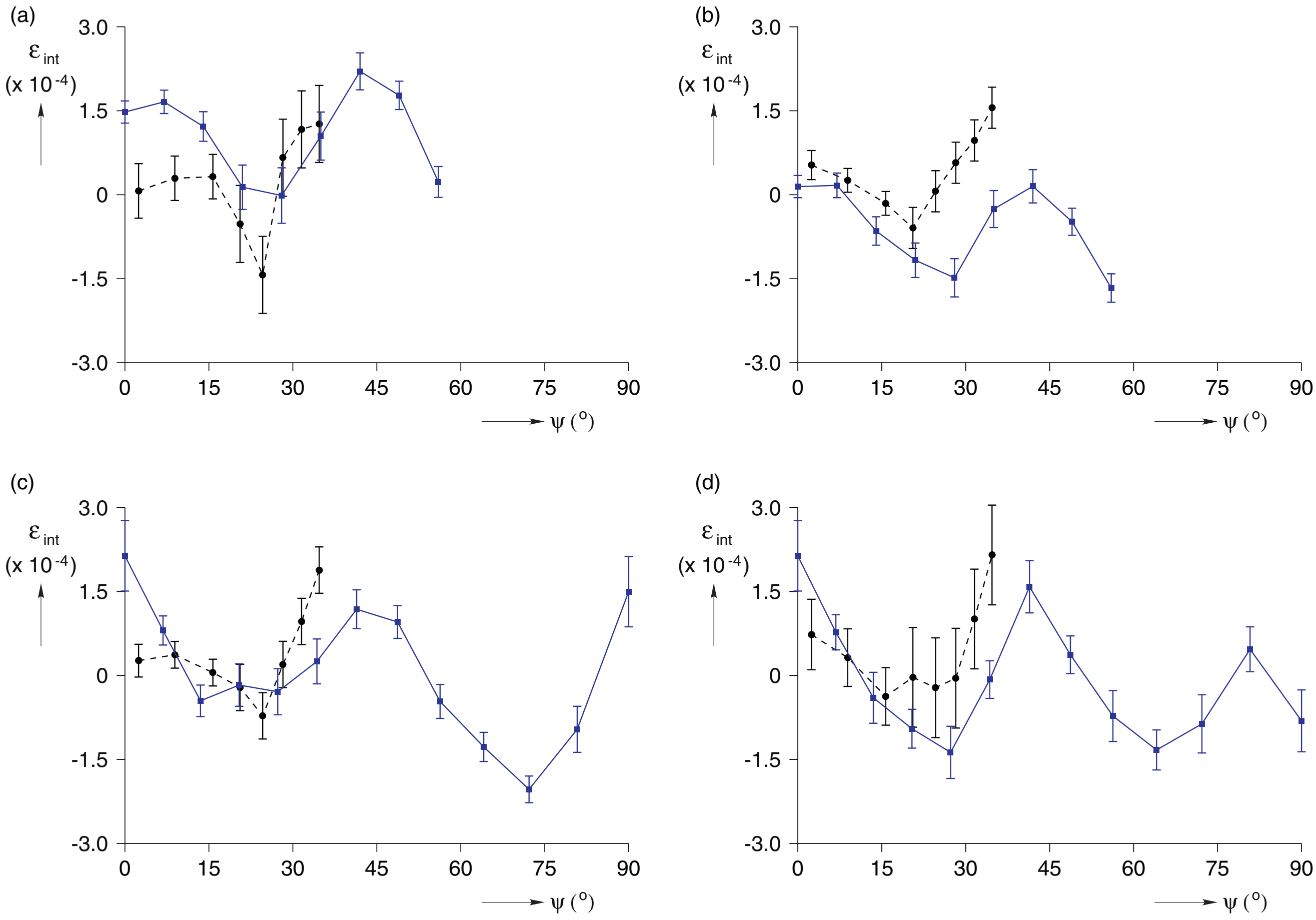

Fig. 8. Average intergranular strains for {4 2 0} plane spacing after equal-biaxial straining calculated from calibration data (dashed lines for equal-biaxial 20% strain) compared with those measured by Euler goniometer XRD system (solid lines for equal-biaxial 26% strain) measurements in (a) RD and (b) TD. Neutron diffraction measurements (solid lines) and average intergranular strains calculated from effective XEC data (dashed lines) in (c) RD and (d) TD for equal-biaxial 5% strained samples. Note the larger ψ range than Fig. 7.

Author's personal copy

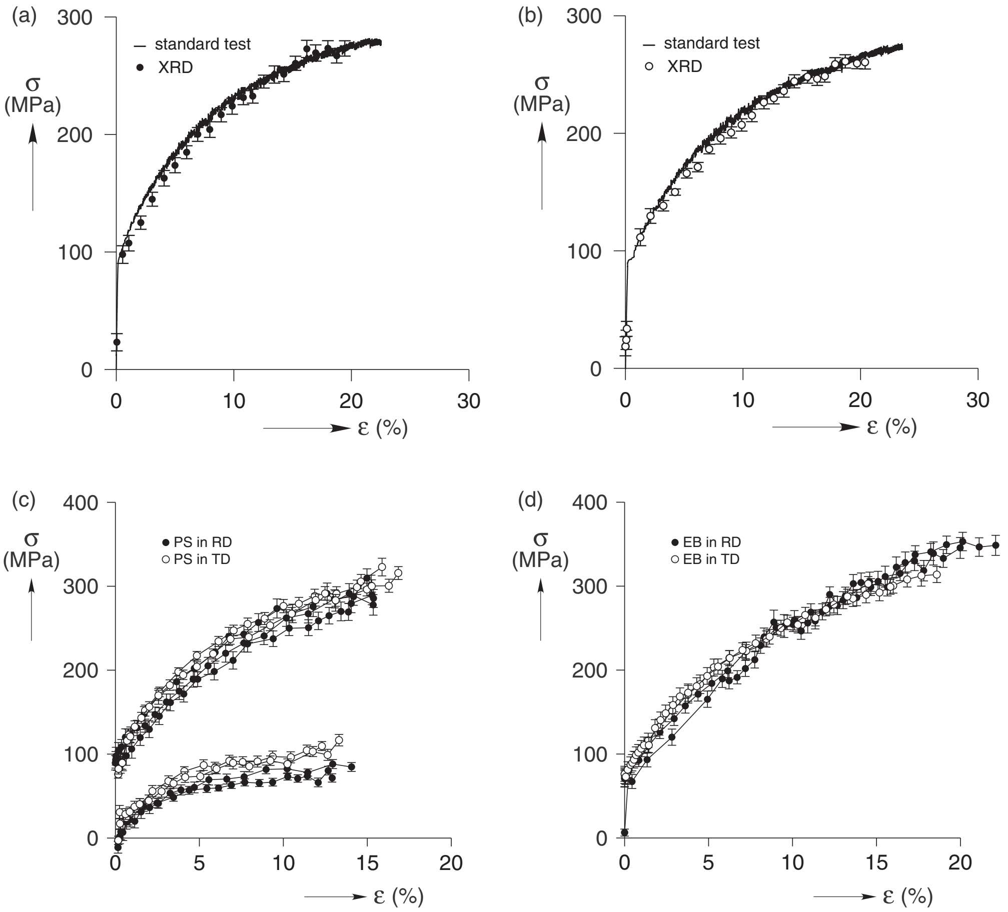

Fig. 9. Calibrated XRD uniaxial stress–strain results from Iadicola et al. [1] in (a) RD and (b) TD with standard uniaxial curves (solid lines). Biaxial XRD stress–strain results from Iadicola et al. [1] for (c) plane-strain and (d) equal-biaxial deformation, with RD and TD plotted in closed and open circles, respectively.

incorporated into the sheet metal forming machine ($\psi = \pm 35^\circ$). These measurements also use Co Kα radiation looking at the spacing of the {4 2 0} family of planes, and the data are plotted in Fig. 8a and b for the RD and TD respectively (solid lines). Symmetry in the $\pm\psi$ range is assumed and the measured data are averaged for equal $|\psi|$ angles. The error bars shown are uncertainties based on the counting statistics of the measurements. Also plotted in Fig. 8a and b are the values calculated from the calibration data for the 20% equal-biaxially strained sample in both directions, where the results have been averaged for $\pm\psi$ symmetry and for $|\psi|$ angles within the $\pm 3^\circ$ scanning oscillation of one another. The error bars are the propagated uncertainties of each average value. The quantitative values agree within the uncertainty of the measurements at only some ψ-angles, but the qualitative variation is quite similar between the calibration data and the values measured using the Euler goniometer. The agreement is quite remarkable considering the Euler goniometer measurements are for an unloaded sample and the effective XEC measurements are extrapolated from results on a loaded sample. The difference could be due in part to the different plastic strain levels where approximately 25% strain level is near to the failure strain.

A second set of measurements over an even larger ψ range (approximately $\psi = \pm 90^\circ$) using neutron diffraction were performed at the NIST Center for Neutron Research. Again the {4 2 0} family of planes was measured and the results are plotted (solid lines) in Fig. 8c and d in the RD and TD respectively for an unloaded 5% equal-biaxially strained sample. The error bars are based on the counting statistics of each diffraction peak. These data are averaged results assuming symmetry in positive and negative ψ-axis. The values calculated from the effective XEC calibration data for a 5% equal-biaxially strained sample in both directions are plotted in dashed lines. Again the calculated values assume symmetry in $\pm\psi$ and are averaged for $|\psi|$ angles within $\pm 3^\circ$ of one another. The neutron results quantitatively match the calibration measurement results for only a small range of angles. However, the qualitative variation is similar, and the ψ locations of the intergranular strain minimums are similar. Only the neutron measurements show a peak at $\psi = 0^\circ$, whereas both XRD methods show a leveling off at this angle.

Considering the uncertainties associated with the effective XEC XRD measurements and that they are performed over a smaller ψ range it is not surprising that the measurements do not capture the intergranular behavior as well as the other two methods, but the fact that it does capture the trends using a test method not specifically intended to measure intergranular stress without a full unloading is very impressive. It must be emphasized that X-ray and neutron diffraction differ in one important aspect: depth penetration which is about 10^3 times larger for neutrons. As a result, in X-ray diffraction the number of contributing grains is by the same factor smaller, and, because of the shallow penetration, it is subject to possible through thickness differences stemming from the initial rolling texture or a lack of constraining grains at the surface. This may explain the difference described above between the XRD and neutron values at $\psi = 0^\circ$.

Similar to above, the $(1/2)S_2$ values were recalculated adjusting the data by subtraction of the intergranular strains measured by the alternate methods. The recalculated values again showed minimal

Author's personal copy

change in the effective XECs with plastic strain, therefore intergranular stresses do not seem to significantly affect our effective XEC determination. One possible reason is that large range of stress over which the effective XEC is being measured out weighs the comparatively small intergranular stresses. Additionally since the biaxial stress–strain measurements are made in a consistent way with the effective XEC measurements, it is likely that any minor offsets in strain or angle will effect both sets of data equally and therefore be corrected through the self-consistent calibration method described here.

4.3. Macro scale stress–strain data comparison

Stress–strain curves from standard uniaxial fixed rate tests [1] are shown in Fig. 9a and b for the RD and TD, respectively, along with data points measured by XRD using the average $(1/2)S_2$ values described above. The XRD data coincide well with the standard test results, with some variation at lower strain levels (especially for the RD). The results for the XRD plane-strain and equal-biaxial experiments [1] calculated using the same $(1/2)S_2$ values are plotted in Fig. 9c and d. The plane-strain stress data for the near-zero strain direction are plotted using the strain in the maximum (principal) strain direction for visibility. Each plot includes data from two data sets performed months apart by different system operators to check measurement repeatability. With the exception of one RD equal-biaxial data point (at about 2.7% strain) the repeat tests agree well. See Iadicola et al. [1] for explanation of measured uncertainties. A more complicated calibration using the variation of $(1/2)S_2$ with stress level (as shown in Fig. 4a) could be used. This more complicated calibration would slightly increase the measured stress values at lower stress levels and slightly decrease the measured stresses at the higher stress levels, which may correct the minor differences seen in Fig. 9a and b. Overall the calibration method produces useful biaxial stress–strain data for sheet metal samples through very high levels of plastic strain, previously unattainable.

5. Summary and conclusion

Combined uniaxial and in situ X-ray diffraction experiments were performed to calibrate the effective X-ray elastic constants for use in other experiments. The results of almost 70 uniaxial effective X-ray elastic constant experiments were presented. These experiments were performed on a single aluminum alloy of interest that had been plastically deformed either through either uniaxial or equal-biaxial tension, and the effective X-ray elastic constants were measured in the sheet rolling and transverse directions. The results show that the X-ray elastic constant for the rolling direction was slightly higher than that of the transverse direction. They also show that there is a trend for the elastic constants to increase slightly with increased uniaxial or equal-biaxial plastic deformation. It was not clear from the data if this trend is more closely associated with the increase in hardening stress level or the plastic strain. The possibility of intergranular stresses causing nonlinear behavior in the $\sin^2\psi$ technique was investigated. The measured intergranular strains seemed to be most prevalent in the equal-biaxial plastically strained samples, which were the only cases with a large enough effect to be measured using the less sensitive X-ray system associated with the mechanical testing. The effect of the intergranular strains on the X-ray elastic constants was found to be minor. The measured average effective X-ray elastic constants were used to calibrate separate uniaxial test of as-received samples, and the results compared very well with the results from standard testing. These same constants were used to calibrate uniaxial, plane-strain, and equal-biaxial data associated with another study [1].

References

[1] M.A. Iadicola, T. Foecke, S.W. Banovic, International Journal of Plasticity 24 (2008) 2084–2101.
[2] M.A. Iadicola, T.H. Gnaeupel-Herold, Advances in X-ray Analysis 51 (2008) 131–137.
[3] K.S. Raghavan, Metallurgical and Materials Transactions A 26A (8) (1995) 2075–2084.
[4] Z. Marciniak, K. Kuczynski, International Journal of Mechanical Science 9 (1967) 609–620.
[5] T. Foecke, M.A. Iadicola, A. Lin, S.W. Banovic, Metallurgical and Materials Transactions A 38 (2007) 306–313.
[6] I.C. Noyan, J.B. Cohen, Residual Stress, Springer-Verlag, New York, 1987.
[7] T. Gnäupel-Herold, A. Creuziger, M. Iadicola, Journal of Applied Crystallography 45 (2012) 197–206.
[8] J.S. Kallend, U.F. Kocks, A.D. Rollett, H.-R. Wenk, Materials Science and Engineering A 132 (1991) 1–11.
[9] H. Behnken, Physica Status Solidi (A) 177 (2000) 401–418.